Analysis of Linear Non-Destructive Testing and Evaluation Methods for Thin-Walled Structure Inspection Using Ultrasonic Array

Yang Li *, Zhenggan Zhou and Jun Wang

School of Mechanical Engineering and Automation, Beihang University, Beijing 100083, China; zzhenggan@buaa.edu.cn (Z.Z.); sy1707512@buaa.edu.cn (J.W.)

* Correspondence: by1107113@buaa.edu.cn

Abstract: The ultrasonic array used for thin-walled structure non-destructive inspection usually has a high central frequency so that the thickness-to-acoustic wavelength ratio is greater than 10. When the ratio is much smaller than 10, the reliability of the conventional ultrasonic array method will dramatically decrease due to the influence of the acoustic near-field. This situation is unavoidable since the available central frequency of the array transducer cannot be an arbitrarily large value. To optimize the inspection performance in this case, the testing of an ultrasonic array and the evaluation of a structure whose thickness is smaller than five-times the longitudinal wavelength are analyzed in this paper. Linear ultrasonic array methods using different combinations of wave patterns, reflection times, and coupling conditions are uniformly expressed as full matrix algorithms. Simulated and experimental full matrices of 6 mm-thick aluminum plates using a 5-MHz array transducer are captured to analyze their imaging performances and sizing abilities with respect to various defects. Analyses show that the inspection results of the wedge coupling method have a much higher signal-to-noise ratio (SNR) than the results of conventional direct contact methods. Circular defects and rectangular defects can be distinguished by comparing the imaging results of different modes. For the simulated circular defect, the diameter can be measured according to the maximum image amplitude of the defect. To simulate a rectangular defect located in the lower half of the region, the nominal length can be measured using a linear function whose input is a −6 dB drop in length of the SS-S mode image. For a real sample, the material anisotropy and complex self-reflections will decrease the SNR by about 10 dB.

Keywords: ultrasonic array; full matrix; multi-mode total focusing method; thin-walled structure

1. Introduction

The light-weight design and manufacture of components are among the most important topics in industries such as aerospace, military, and automotive. The most effective approach is to use a thin-walled structure, like grid fins in aerospace. To monitor the integrity and status of components during their total lifecycle, appropriate non-destructive testing and evaluation (NDT&E) methods are required to find the potential interior flaws, such as holes and cracks. NDT&E methods like infrared [1,2] are very sensitive to surface defects and can be applied in the far-field without any environmental impact. However, it is not sensitive to inner defects. Computed Tomography (CT) [3] has very high imaging resolution for volume-type defects like holes. However, it is not sensitive to two-dimensional discontinuities like cracks, and the radiation is harmful to the human body. The ultrasonic method [4] is one of the most promising NDT&E methods without any environmental impact or harm. Defects inside a sample can be located and sized directly using the A-scan

signal received by a single-element ultrasonic transducer. It is very sensitive to both volume and two-dimensional defects in elastic materials. For a thin-walled structure, unfortunately, its thickness and acoustic wavelength may have the same order of magnitude, so the effect of the acoustic near-field cannot be ignored [5]. In this case, the complex near-field will increase the difficulties of the A-scan signal interpretation and the miss rate during ultrasonic inspection.

There are two practical methods to overcome the interference of the acoustic near-field:

- Slant the transducer to a specific angle so that the emitted acoustic wave in coupling materials like fluid or a wedge can propagate along an oblique ray path into the sample [6]. The interaction between the ultrasound and the reflector within the near-field can then be neglected since the length of the inclined acoustic ray becomes larger than the near-field length. Transducers with different focal lengths are needed to improve the inspection resolution along the acoustic ray since a conventional single-element ultrasonic transducer has a constant focal length. On the other hand, the inclined angle has to be varied within a certain range to ensure the full coverage of the inspection region. The above descriptions show that thin-walled structure inspection using a single-element ultrasonic transducer has very low efficiency and resolution.

- Replace the conventional transducer with an ultrasonic array so that the acoustic ray can be steered toward an arbitrary expected direction without any physical transducer movement [7]. The steering angle of the acoustic ray is controlled by the transmission and reception delay of each array element. Due to the powerful beam control ability, ultrasonic array methods have much higher resolution and flexibility compared with single-element methods. Coupling materials can be used as well to optimize the wave pattern and the directivity of the acoustic ray. The above descriptions show that thin-walled structure inspection using an ultrasonic array is more preferable.

Current research works on thin-walled structure inspection have been mainly conducted using array transducers with a high central frequency. For a 6 mm-thick titanium thin-walled structure with a 6000-m/s longitudinal wave velocity, direct contact testing and evaluation using array transducers, whose central frequency is greater than 10 MHz, have been analyzed in detail [8]. In this case, the thickness of the structure is greater than 10-times the longitudinal wavelength. However, there are few research works discussing the situation when the thickness-to-wavelength ratio is much smaller than 10. Unfortunately, due to the manufacturing technology and cost restrictions, the thicknesses of many thin-walled structures will be smaller than 10-times the minimum longitudinal wavelength of the available array transducer. The aim of this paper is to analyze the performance of the linear ultrasonic array methods for a thin-walled structure whose thickness is smaller than five-times the longitudinal wavelength. In Section 2, ultrasonic array methods for thin-walled structure inspection will be described using a full matrix. In Section 3, a full matrix capture of 6 mm-thick thin-walled aluminum plates using a 5-MHz linear array will be simulated based on the finite difference time domain (FDTD) method. These plates are embedded with defects of different geometrical types. Defect location, maximum defect image amplitude, defect sizing ability, and defect SNR (DSNR) are used to analyze their performances theoretically. In Section 4, linear ultrasonic array methods are applied to real aluminum welding structures with side-drilled holes (SDH) and electric discharge-machined (EDM) notches.

2. Linear Ultrasonic Array Method for a General Thin-Walled Structure

In the following descriptions, a series of symbols listed in Table 1 will be used.

Table 1. Symbols of the thin-walled structure and array transducer.

Symbol	Meaning
c_1	Longitudinal wave velocity in the wedge
c_{2L}	Longitudinal wave velocity in the thin-walled structure
c_{2S}	Shear wave velocity in the thin-walled structure
H	Thickness of the thin-walled structure
N	Element count of the ultrasonic array transducer
x_{ti}	x coordinate of array element i ($1 \leq i \leq N$)
z_{ti}	z coordinate of array element i ($1 \leq i \leq N$)

The set of all possible signals generated by the linear ultrasonic array can be abstractly regarded as a linear vector space whose basis set is a full matrix. Full matrix $\{m_{ij}(t)|i, j = 1, 2, ..., N\}$ is the complete set of time-domain data from all transmit and receive elements' combinations. To unify the analysis framework, linear ultrasonic array methods in this paper are all identified as data processing algorithms of analytical complex data $\{M_{ij}(t)|i, j = 1, 2, ..., N\}$, which is the Hilbert transformation result of the full matrix [9]. Mode conversion and reflection of the acoustic ray inside the thin-walled structure can be abstractly regarded as a ray-tracing problem in a multi-layered medium. As shown in Figure 1, the acoustic ray traveling to a specific point in the sample after $n - 1$ times of reflection is equivalent to the transmission through $n + 1$ layered material. Layer 0 is the coupling material. The terms "LSSL" and "SSL" illustrate the wave mode constitutions of acoustic ray in sample. The capital "L" refers to longitudinal wave and the capital "S" refers to shear wave. The thicknesses of Layers 1–n are all equal to the thickness of the sample. The wave velocity in layer $i + 1$ is determined by the selected wave pattern after i times of reflection. To unify the ray-tracing procedure, function $\text{TOF}_n(x_0, z_0, x_1, z_1, \{c_i\}_{i=0}^{n}, \{h_i\}_{i=1}^{n-1})$ is defined to solve the time of flight from point (x_0, z_0) in Layer 0 to point (x_1, z_1) in layer n, where set $\{c_i\}_{i=0}^{n}$ denotes the wave velocity distribution from Layers 0–n, and set $\{h_i\}_{i=1}^{n-1}$ denotes the thickness distribution from Layers 1–$n - 1$. Function TOF_n can be numerically solved using Snell's law or the Fermat minimum principle [10,11].
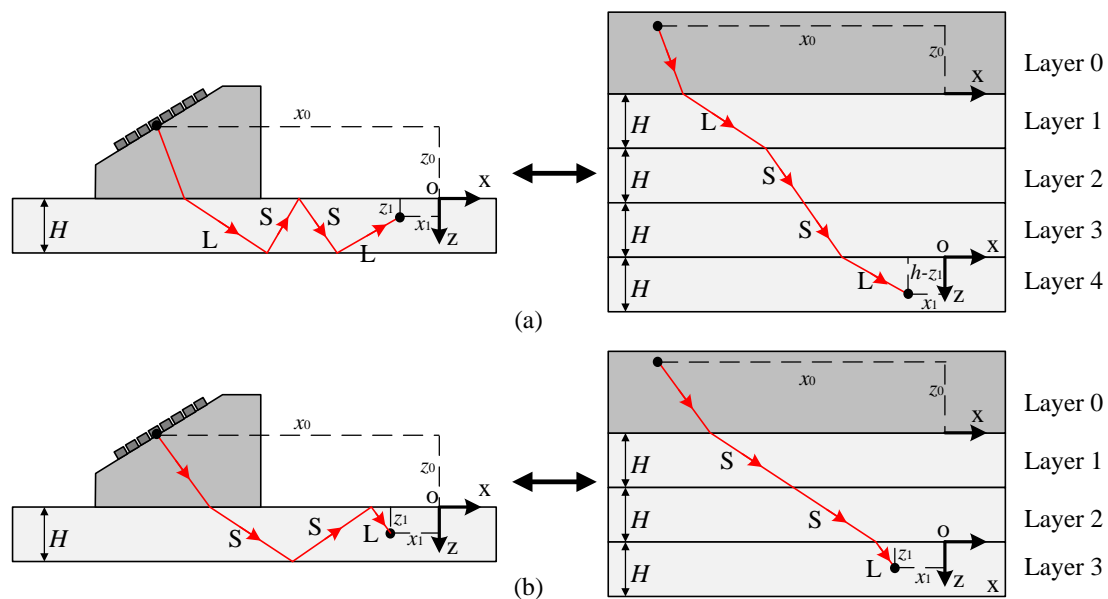
Figure 1. Ray tracing through a multi-layered medium: (**a**) Path LSSL; (**b**) Path SSL.

2.1. Phased Array Method

The control of the phased array beam can be achieved by making the peak amplitude of ultrasound emitted from each activated array element occurred in the focal point simultaneously. The reception of the reflection wave can be accomplished in the same way according to the acoustic reciprocity principle. The A-scan signal $s(t)$ of the phased array beam focused at point (x_f, z_f) can be expressed as:

$$\begin{cases} s(t) = \sum_{i \in AP_T} \sum_{j \in AP_R} M_{ij}(t - \Delta t_{Ti} - \Delta t_{Rj}) \\ \Delta t_{Ti} = \max(\{T_{Ti}\}_{i \in AP_T}) - T_{Ti} \\ \Delta t_{Rj} = \max(\{T_{Rj}\}_{j \in AP_R}) - T_{Rj} \end{cases} \tag{1}$$

where $\{T_{Ti}\}_{i \in AP_T}$ and $\{T_{Rj}\}_{j \in AP_R}$, the delay laws of transmitted and received apertures AP_T and AP_R, can be calculated by function TOF_n. If the mode of the phased array beam used in thin-walled structure inspection is LSSL-SSL, then T_{Ti} and T_{Rj} of activated elements i and j can be expressed as:

$$\begin{cases} T_{Ti} = TOF_4(x_{ti}, z_{ti}, x_f, H - z_f, a_i, b_i) \\ T_{Rj} = TOF_3(x_{tj}, z_{tj}, x_f, z_f, a_j, b_j) \\ a_i = \{H, H, H\}, b_i = \{c_1, c_{2L}, c_{2S}, c_{2S}, c_{2L}\} \\ a_j = \{H, H\}, b_j = \{c_1, c_{2S}, c_{2S}, c_{2L}\} \end{cases} \tag{2}$$

To image a certain region, the phased array solution will contain a finite set of A-scan signals $\{s_k(t)\}_{k=1}^M$. Each A-scan signal corresponds to an element of finite focal point set $\{(x_{f_k}, z_{f_k})\}_{k=1}^M$. The B-scan image can then be expressed as:

$$I_B(k, t) = |s_k(t)| \tag{3}$$

Different focal points and activated aperture distributions correspond to different interpretations of I_B. When the focal point is moved along a non-vertical direction with a fixed activated aperture, I_B happens to be equivalent to the sector B-scan image in polar coordinates. The vertical direction is parallel to the normal vector of the array surface. When the focal point and aperture center are moved along a non-vertical direction simultaneously, I_B happens to be equivalent to the electronic B-scan image in Cartesian coordinates. When the focal point is moved along the vertical direction with fixed activated aperture, I_B happens to be equivalent to the A-scan signal of dynamic depth focuses (DDF).

2.2. Total Focusing Method

The total focusing method (TFM) can be theoretically regarded as the limit of the phased array method when the cardinality of the focal point set tends to infinity. In practical applications, the cardinality is a large positive integer determined by the inspection region and discrete resolution of the image grid. When the sizes of activated apertures AP_T and AP_R are equal to the element count, the TFM image for thin-walled structure inspection can be expressed as:

$$I_{TFM}(x, z) = |\sum_{i=1}^N \sum_{j=1}^N M_{ij}(T_i + T_j)| \tag{4}$$

where T_i and T_j, the time flight of the acoustic ray from array elements i and j to focal point (x, z), can be calculated using Equation (2) as well. The roles of T_i and T_j in TFM image formula Equation (4) are similar to the delay term Δt in phased array A-scan signal formula Equation (1).

When the array transducer is directly contacted to the sample, the z coordinate of each array element will be set to zero, and the ray path obtained by Equation (2) will be reduced to Equation (11) in Zhang's paper [12]. Without the existence of acoustic wave reflection or transmission through a coupling interface, the interpretation of the TFM image becomes much easier. However, the following two reasons show that the usage of coupling materials like a wedge is a necessary condition for thin-walled structure inspection:

- The array transducer may have problems with direct coupling and abrasion if the sample has a rough surface.
- The shear wave component of the full matrix is hardly used. According to the directivity of the elastic wave generated by directly contacting the single-element transducer [13], most of the shear wave energy belongs to interval $[45°, 90°]$. The shear wave of defects contained in the A-scan signal may have a very low SNR and additional artifacts due to the unneglectable grating lobes when the steering angle of the ultrasonic array beam is greater than $45°$ [14,15].

In the following analyses, only TFM is considered, since it has better resolution compared with finite focus phased array methods. Each ultrasonic array method corresponds to a specific TFM imaging mode. The term mode refers to the specific combination of wave patterns, reflection time combinations, and coupling conditions of Equation (4). TFM results of different modes are analyzed by their imaging performances and sizing abilities with respect to various defects.

3. Theoretical Analysis

The simulation of full matrix capture (FMC) is required to analyze the performance of thin-walled structure inspection theoretically using different ultrasonic array methods. Available tools for dynamic elastic field calculation include semi-analytical, finite element (FE), and FDTD. A hybrid model [16,17] is frequently used to analyze the full matrix and TFM of the direct contact array transducer. The analytical solution of the point source and FE were combined to calculate the ray path and scattering field, respectively. In order to model the transmission and reflection through the coupling interface correctly and efficiently, FDTD was used in this paper. The simulation program was established based on C++ and CUDA [18].

3.1. FDTD Model

FMC of the linear ultrasonic array can be simplified to a two-dimensional problem. A first order difference scheme with a perfect matching absorbing layer was selected in consideration of accuracy, stability, speed, and multi-medium coupling. This scheme can be expressed as [19]:

$$
\begin{cases}
v_x|_{i-1/2,k}^{n+1/2} = v_{x1}|_{i-1/2,k}^{n+1/2} + v_{x2}|_{i-1/2,k}^{n+1/2}, v_z|_{i,k-1/2}^{n+1/2} = v_{z1}|_{i,k-1/2}^{n+1/2} + v_{z2}|_{i,k-1/2}^{n+1/2} \\
\sigma_{xx}|_{i,k}^{n+1} = \sigma_{xx1}|_{i,k}^{n+1} + \sigma_{xx2}|_{i,k}^{n+1}, \sigma_{zz}|_{i,k}^{n+1} = \sigma_{zz1}|_{i,k}^{n+1} + \sigma_{zz2}|_{i,k}^{n+1} \\
\sigma_{xz}|_{i-1/2,k-1/2}^{n+1} = \sigma_{xz1}|_{i-1/2,k-1/2}^{n+1} + \sigma_{xz2}|_{i-1/2,k-1/2}^{n+1} \\
v_{x1}|_{i-1/2,k}^{n+1/2} = C_{vxx1}|_{i,k}(\sigma_{xx}|_{i,k}^{n} - \sigma_{xx}|_{i-1,k}^{n}) + C_{vxx2}|_{i,k}v_{x1}|_{i-1/2,k}^{n-1/2} \\
v_{x2}|_{i-1/2,k}^{n+1/2} = C_{vxz1}|_{i,k}(\sigma_{xz}|_{i-1/2,k+1/2}^{n} - \sigma_{xz}|_{i-1/2,k-1/2}^{n}) + C_{vxz2}|_{i,k}v_{x2}|_{i-1/2,k}^{n-1/2} \\
v_{z1}|_{i,k-1/2}^{n+1/2} = C_{vzx1}|_{i,k}(\sigma_{xz}|_{i+1/2,k-1/2}^{n} - \sigma_{xz}|_{i-1/2,k-1/2}^{n}) + C_{vzx2}|_{i,k}v_{z1}|_{i,k-1/2}^{n-1/2} \\
v_{z2}|_{i,k-1/2}^{n+1/2} = C_{vzz1}|_{i,k}(\sigma_{zz}|_{i,k}^{n} - \sigma_{zz}|_{i,k-1}^{n}) + C_{vzz2}|_{i,k}v_{z2}|_{i,k-1/2}^{n-1/2} \\
\sigma_{xx1}|_{i,k}^{n+1} = C_{txx1}|_{i,k}(v_x|_{i+1/2,k}^{n+1/2} - v_x|_{i-1/2,k}^{n+1/2}) + C_{txx2}|_{i,k}\sigma_{xx1}|_{i,k}^{n} \\
\sigma_{xx2}|_{i,k}^{n+1} = C_{txz1}|_{i,k}(v_z|_{i,k+1/2}^{n+1/2} - v_z|_{i,k-1/2}^{n+1/2}) + C_{txz2}|_{i,k}\sigma_{xx2}|_{i,k}^{n} \\
\sigma_{zz1}|_{i,k}^{n+1} = C_{tzx1}|_{i,k}(v_x|_{i+1/2,k}^{n+1/2} - v_x|_{i-1/2,k}^{n+1/2}) + C_{tzx2}|_{i,k}\sigma_{zz1}|_{i,k}^{n} \\
\sigma_{zz2}|_{i,k}^{n+1} = C_{tzz1}|_{i,k}(v_z|_{i,k+1/2}^{n+1/2} - v_z|_{i,k-1/2}^{n+1/2}) + C_{tzz2}|_{i,k}\sigma_{zz2}|_{i,k}^{n} \\
\sigma_{xz1}|_{i-1/2,k-1/2}^{n+1} = C_{txzx1}|_{i,k}(v_z|_{i,k-1/2}^{n+1/2} - v_z|_{i-1,k-1/2}^{n+1/2}) + C_{txzx2}|_{i,k}\sigma_{xz1}|_{i-1/2,k-1/2}^{n} \\
\sigma_{xz2}|_{i-1/2,k-1/2}^{n+1} = C_{txzz1}|_{i,k}(v_x|_{i-1/2,k}^{n+1/2} - v_x|_{i-1/2,k-1}^{n+1/2}) + C_{txzz2}|_{i,k}\sigma_{xz2}|_{i-1/2,k-1/2}^{n}
\end{cases}
\tag{5}
$$

and

$$
\begin{cases}
C_{vxx1}|_{i,k} = 2/\overline{\rho_x}|_{i,k}(2 + \Delta t \overline{dx}|_{i,k}), C_{vxx2}|_{i,k} = (2 - \Delta t \overline{dx}|_{i,k})/(2 + \Delta t \overline{dx}|_{i,k}) \\
C_{vxz1}|_{i,k} = 2/\overline{\rho_x}|_{i,k}(2 + \Delta t dz|_{i,k}), C_{vxz2}|_{i,k} = (2 - \Delta t dz|_{i,k})/(2 + \Delta t dz|_{i,k}) \\
C_{vzx1}|_{i,k} = 2/\overline{\rho_z}|_{i,k}(2 + \Delta t dx|_{i,k}), C_{vzx2}|_{i,k} = (2 - \Delta t dx|_{i,k})/(2 + \Delta t dx|_{i,k}) \\
C_{vzz1}|_{i,k} = 2/\overline{\rho_z}|_{i,k}(2 + \Delta t \overline{dz}|_{i,k}), C_{vzz2}|_{i,k} = (2 - \Delta t \overline{dz}|_{i,k})/(2 + \Delta t \overline{dz}|_{i,k}) \\
C_{txx1}|_{i,k} = 2C_{11}|_{i,k}/(2\Delta h/\Delta t + dx|_{i,k}), C_{txx2}|_{i,k} = (2 - \Delta t dx|_{i,k})/(2 + \Delta t dx|_{i,k}) \\
C_{txz1}|_{i,k} = 2C_{13}|_{i,k}/(2\Delta h/\Delta t + dz|_{i,k}), C_{txz2}|_{i,k} = (2 - \Delta t dz|_{i,k})/(2 + \Delta t dz|_{i,k}) \\
C_{tzx1}|_{i,k} = 2C_{31}|_{i,k}/(2\Delta h/\Delta t + dx|_{i,k}), C_{tzx2}|_{i,k} = (2 - \Delta t dx|_{i,k})/(2 + \Delta t dx|_{i,k}) \\
C_{tzz1}|_{i,k} = 2C_{33}|_{i,k}/(2\Delta h/\Delta t + dz|_{i,k}), C_{tzz2}|_{i,k} = (2 - \Delta t dz|_{i,k})/(2 + \Delta t dz|_{i,k}) \\
C_{txzx1}|_{i,k} = 2/\overline{C_{55}}|_{i,k}((2\Delta h/\Delta t + \overline{dx}|_{i,k}), C_{txzx2}|_{i,k} = (2 - \Delta t \overline{dx}|_{i,k})/(2 + \Delta t \overline{dx}|_{i,k}) \\
C_{txzz1}|_{i,k} = 2/\overline{C_{55}}|_{i,k}((2\Delta h/\Delta t + \overline{dz}|_{i,k}), C_{txzz2}|_{i,k} = (2 - \Delta t \overline{dz}|_{i,k})/(2 + \Delta t \overline{dz}|_{i,k}) \\
\overline{\rho_x}|_{i,k} = (\rho|_{i-1,k} + \rho|_{i,k})\Delta h/2\Delta t, \overline{\rho_z}|_{i,k} = (\rho|_{i,k-1} + \rho|_{i,k})\Delta h/2\Delta t \\
\overline{C_{55}}|_{i,k} = 4/(1/C_{55}|_{i,k} + 1/C_{55}|_{i-1,k} + 1/C_{55}|_{i,k-1} + 1/C_{55}|_{i-1,k-1})
\end{cases}
\tag{6}
$$

where Δt and Δh are the discrete steps of time and space; (i,k) is the index of the rectangle mesh, n is the index of time; v_x, v_z, σ_{xx}, σ_{zz}, and σ_{xz} are the velocity and stress fields of the elastic medium; C_{11}, C_{13}, C_{31}, C_{33}, and C_{55} are the elastic coefficients determined by longitudinal wave velocity c_L, shear wave velocity c_S, and density ρ in an isotropic material. dx and dz are the decay coefficients of the absorbing layer with a non-zero value around the boundary, as shown in Figure 2.
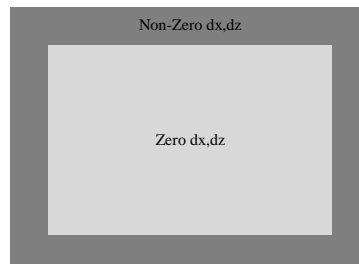

Figure 2. Absorbing layer of the finite difference time domain (FDTD) scheme.

Figure 3a gives the illustration of a real inclined wedge used in the thin-walled structure inspection. The undesirable reflection wave from the coupling interface will be completely absorbed by the material in front of the wedge. To eliminate the influence of wedge reflection in the simulation result as well, a modified wedge model was used, as shown in Figure 3b. In this model, the front of wedge E_1 was extended so that the reflection wave from interface I_1, denoted by the red line, will travel to the absorbing boundary layer of the simulation region after several times of reflection and finally be absorbed. Edge E_2 had a non-zero angle to prevent the additional transmission of the wave through itself. The angle of edge E_2 was required to be much smaller than the wedge angle to avoid back-reflection.

The simulation configurations of FMC on 6 mm-thick aluminum plates using a 32-element 5-MHz linear array with a 0.6-mm pitch are illustrated in Figure 4a,b. The longitudinal wave velocity in the wedge was 2337 m/s. The longitudinal and shear wave velocities in aluminum were 6330 m/s and 3080 m/s. It is easy to check that their thicknesses were indeed smaller than five-times the longitudinal wavelength. Each sample was embedded with an artificial defect of a specific geometrical type, size, and base point combination, as listed in Table 2. The base point of the defect was determined by its center G_0 or G_1, as shown in Figure 4c. If the z-coordinate of the center was smaller than 3 mm, the base point was defined as G_1 or G_4. if the z-coordinate of the center was greater than 3 mm, the base point was defined as G_2 or G_5. In the remaining case, the base point was then defined as G_0 or G_3. The discrete steps of time and space were 5 ns and 0.05 mm, satisfying Courant's condition [20].
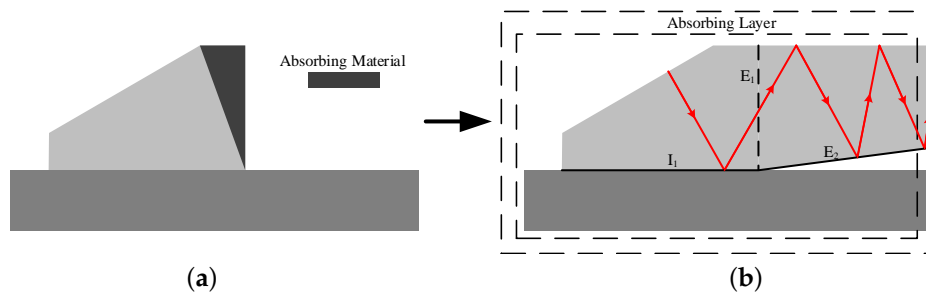
Figure 3. Illustration of the wedge: (**a**) real wedge with sound-absorbing material; (**b**) modified wedge mode for simulation.
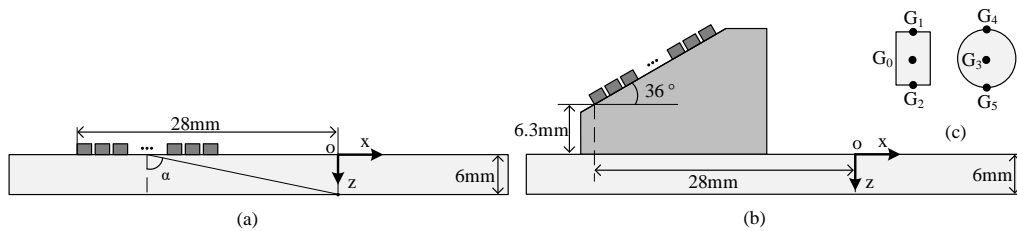
Figure 4. Full matrix capture (FMC) simulation configuration: (**a**) direct contact; (**b**) coupling with inclined wedge; (**c**) embedded defects.

Table 2. Parameters of the embedded artificial defect.

Type	Size	Base Point	Type	Size	Base Point
	0.5 mm × 0.3 mm	(0 mm, 0 mm)		Φ0.4 mm	(0 mm, 0 mm)
	0.75 mm × 0.3 mm	(0 mm, 1 mm)		Φ0.6 mm	(0 mm, 1 mm)
	1 mm × 0.3 mm	(0 mm, 2 mm)		Φ0.8 mm	(0 mm, 2 mm)
Rectangle	1.25 mm × 0.3 mm	(0 mm, 3 mm)	Circle	Φ1 mm	(0 mm, 3 mm)
	1.5 mm × 0.3 mm	(0 mm, 4 mm)		Φ1.2 mm	(0 mm, 4 mm)
	1.75 mm × 0.3 mm	(0 mm, 5 mm)		Φ1.4 mm	(0 mm, 5 mm)
	2 mm × 0.3 mm	(0 mm, 6 mm)		Φ1.6 mm	(0 mm, 6 mm)

In Sections 3.2 and 3.3, the simulation results of direct contact and wedge coupling are analyzed, respectively. Firstly, the indicator DSNR was used to evaluate the imaging performance. DSNR is expressed as:

$$\text{DSNR} = 20log(A_{\max}/\bar{A}) \tag{7}$$

where $A_{\max}$ is the maximum image amplitude of the defect and $\bar{A}$ is the average image amplitude of the background, which is a 6 mm × 6 mm box region surrounding the defect. Secondly, imaging results with the best performance will be used to evaluate their sizing abilities. For symmetry modes like SS-SS, the maximum image amplitude will be used to characterize the size of the defect. For asymmetry modes like SSS-SS, a −6-dB drop method will be used.

3.2. Analysis of the Direct Contact Result

The shear wave energy generated by the directly-contacted single-array element was mainly distributed in a large angle direction where the influence of the grating lobe can be neglected. Therefore, only longitudinal modes including L-L, LL-L, LL-LL, LLL-LL, and LLL-LLL are considered in this section.

Figure 5 gives the TFM results of circular defects at different base points, whose diameters were all 0.8 mm. The maximum mean value and minimum standard deviation of DSNR both occurred for LLL-LLL mode, as shown in Table 3. Although the DSNR distribution of the LLL-LL mode results was very close to LLL-LLL mode, its imaging performance was worse than LLL-LLL mode since the defects in LLL-LL mode images were distorted, which led to the increment of the standard deviation of about 41%. The distortions appearing in the LLL-LL mode results were the consequence of the fact that the majority acoustic energy received from the circular defect belongs to the normal reflection wave. Theoretically, symmetric modes mainly use the normal reflection wave for defect imaging, while asymmetric modes use the specular reflection wave.

Figure 6 gives the relations between the maximum LLL-LLL mode image amplitude of the circular defect and its nominal diameter at different base points. For a defect close to the upper surface ($z = 0$ mm), the image amplitude increased monotonously with the diameter. However, the curve had a poor linearity due to the inflection point at a diameter of 1 mm. For defects at other base points ($z = 3, 6$ mm), unfortunately, no significant relation existed. The poor linearity and disorders were expected since the diameters were close to the longitudinal wavelength (1.3 mm). The complex acoustic diffraction around this region will have very bad influences on circular defect measurement.
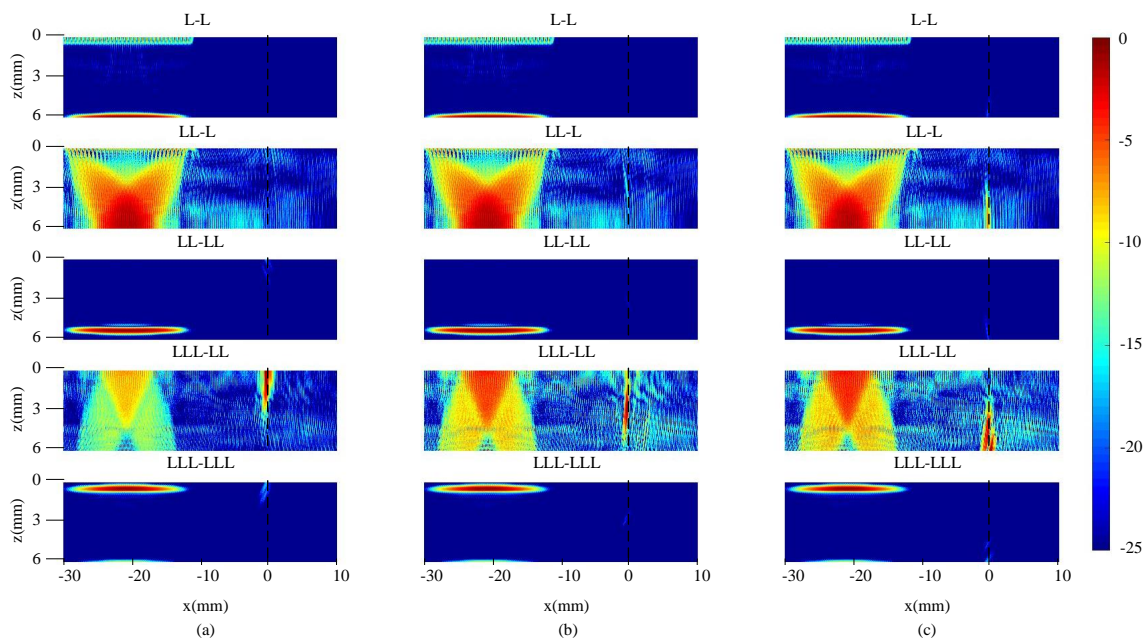
Figure 5. Direct contact total focusing method (TFM) imaging results of circular defects at different base points: (**a**) (0 mm, 0 mm); (**b**) (0 mm, 3 mm); (**c**) (0 mm, 6 mm).

Table 3. Defect SNR (DSNR) of circular defects based on direct contact TFM imaging results.

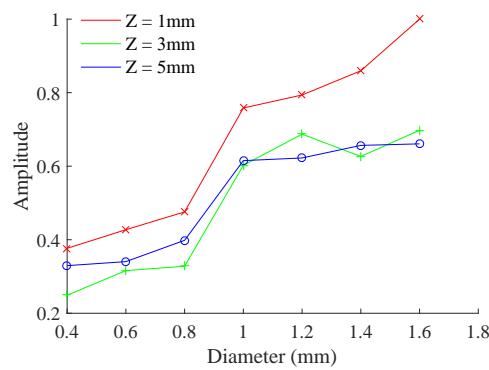| Base Point	L-L	LL-L	LL-LL	LLL-LL	LLL-LLL
(0 mm, 0 mm)	23.90 dB	20.54 dB	37.46 dB	40.33 dB	39.70 dB
(0 mm, 3 mm)	24.3 dB	21.64 dB	31.18 dB	35.99 dB	36.24 dB
(0 mm, 6 mm)	34.00 dB	33.95 dB	35.72 dB	35.44 dB	36.60 dB
Mean	27.41 dB	25.38 dB	34.79 dB	37.25 dB	37.52 dB
Std	5.71 dB	7.45 dB	3.24 dB	2.68 dB	1.90 dB

Figure 6. Plot of the maximum defect image value using the LLL-LLL mode image.

Figure 7 gives the TFM results of rectangular defects at different base points whose sizes were all 1.0 mm × 0.3 mm. The maximum mean value and minimum standard deviation of DSNR both occurred in LLL-LL mode, as shown in Table 4. Although the LLL-LLL mode results had higher DSNR at the upper and lower surface, only a strong root spot accompanied by a weak tip spot could be found. On the other hand, the LLL-LLL mode DSNR of the defect at base point (0 mm, 3 mm) was 28.32 dB, which was much smaller than the 41.62 dB of LLL-LL mode. The occurrences of body part misdetection and weak tip image amplitude when using LLL-LLL mode were the consequence of the fact that the normal reflection was not sensitive to the two-dimensional flat surface. Theoretically, the A-scan signals received from the rectangular defect can be generally divided into three parts: the strong specular reflection, the strong root normal reflection, and the weak tip diffraction. The strong normal reflection of the root could be obtained by symmetry mode only when the defect was extended from the upper (a) or lower (c) surface.
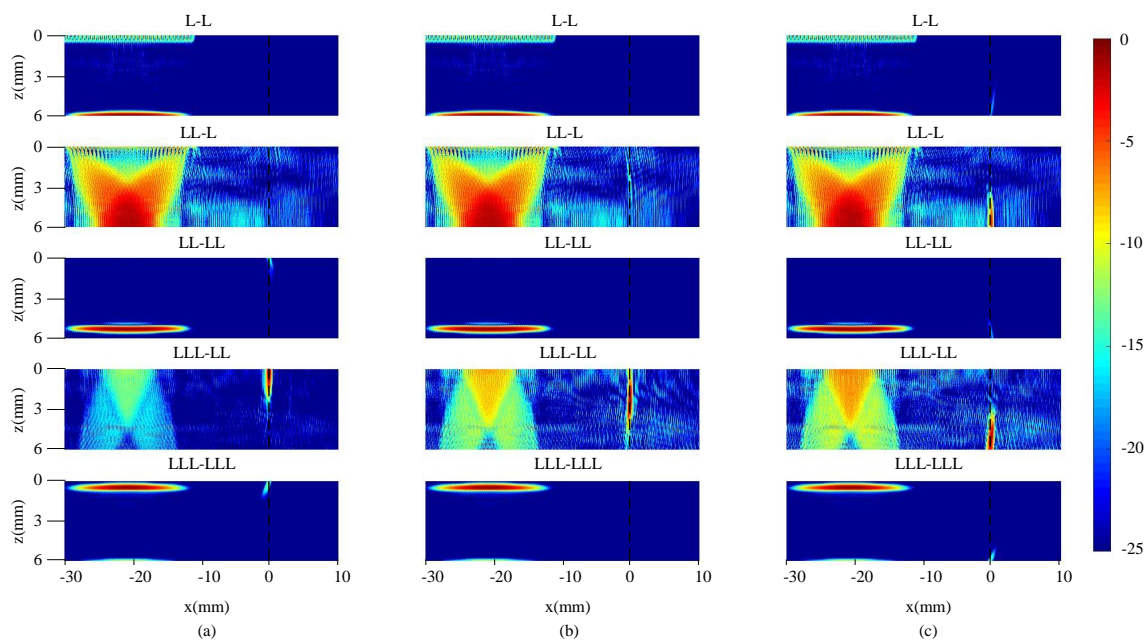

Figure 7. Direct contact TFM imaging results of rectangular defects at different base points: (**a**) (0 mm, 0 mm); (**b**) (0 mm, 3 mm); (**c**) (0 mm, 6 mm).

Table 4. DSNR of rectangular defects based on direct contact TFM imaging results.

Base Point	L-L	LL-L	LL-LL	LLL-LL	LLL-LLL
(0 mm, 0 mm)	23.93 dB	20.95 dB	49.20 dB	51.97 dB	52.25 dB
(0 mm, 3 mm)	23.45 dB	24.02 dB	27.62 dB	41.62 dB	28.32 dB
(0 mm, 6 mm)	40.16 dB	40.03 dB	40.84 dB	44.20 dB	49.21 dB
Mean	29.18 dB	28.34 dB	39.21 dB	45.93 dB	43.26 dB
Std	9.51 dB	10.24 dB	10.88 dB	5.38 dB	13.02 dB

Figure 8a gives the relations between the measured −6-dB drop length of the rectangular defect in the LLL-LL mode image and its nominal length at different base points. The poor monotonicity and great deviation of these curves made the sizing of the rectangular defect much harder. For the rectangular defect extended from the lower surface (z = 6 mm), the measured −6-dB drop length from the LL-L mode image increased monotonously and linearly despite the relatively low DSNR, as shown in Figure 8b. The deviation with respect to the nominal length was mainly due to the excessive angle α (about 75°) between the array center and defect root, as shown in Figure 4a. According to Felice's research [8], the deviation will dramatically increase if α is greater than 65°.
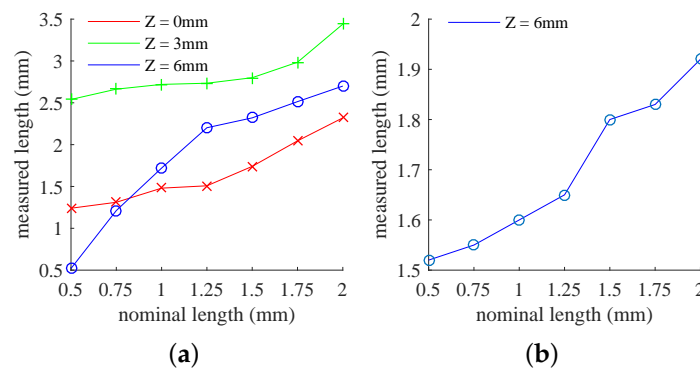

Figure 8. Plot of the measured −6-dB drop length using different imaging modes: (**a**) LLL-LL mode; (**b**) LL-L mode.

The above analyses show that, in the case of direct contact, the best mode for a circular defect is LLL-LLL, and the best mode for a rectangular defect is LLL-LL. Defects with different geometrical types can be distinguished by comparing multi-mode TFM results. When the defect diameter (length) is smaller than 2 mm, direct contact ultrasonic array methods are unable to measure defect size.

3.3. Analysis of the Wedge Coupling Result

The longitudinal wave transmitted through the inclined wedge is weak compared with the shear wave due to the total reflection. Therefore, only shear wave modes including S-S, SS-S, SS-SS, SSS-SS, and SSS-SSS are considered in this section.

Figure 9 gives the TFM results of circular defects at different base points whose diameters were all 0.8 mm. The maximum mean value and minimum standard deviation of DSNR both occurred in SS-SS mode, as shown in Table 5. Unlike direct contact inspection, the imaging results of symmetry modes had significant DSNR differences with asymmetry modes. The highest DSNR values of defects at three base points were all obtained by symmetry modes (z = 0, 6 mm at SS-SS, z = 3 mm at SSS-SSS). The minimum DSNR difference between the best symmetry and the asymmetry mode result was about 6 dB. On the other hand, The mean DSNR of the SS-SS mode was about 10 dB higher than the DSNR of the LLL-LLL mode in Section 3.2.
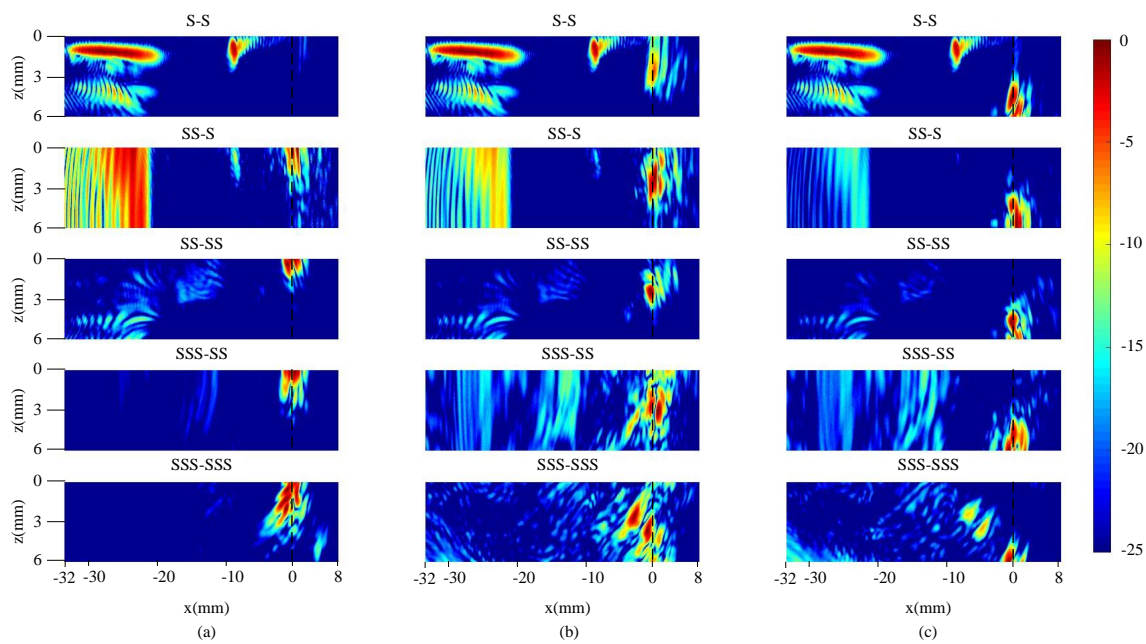
Figure 9. Wedge coupling TFM imaging results of circular defects at different base points: (**a**) (0 mm, 0 mm); (**b**) (0 mm, 3 mm); (**c**) (0 mm, 6 mm).

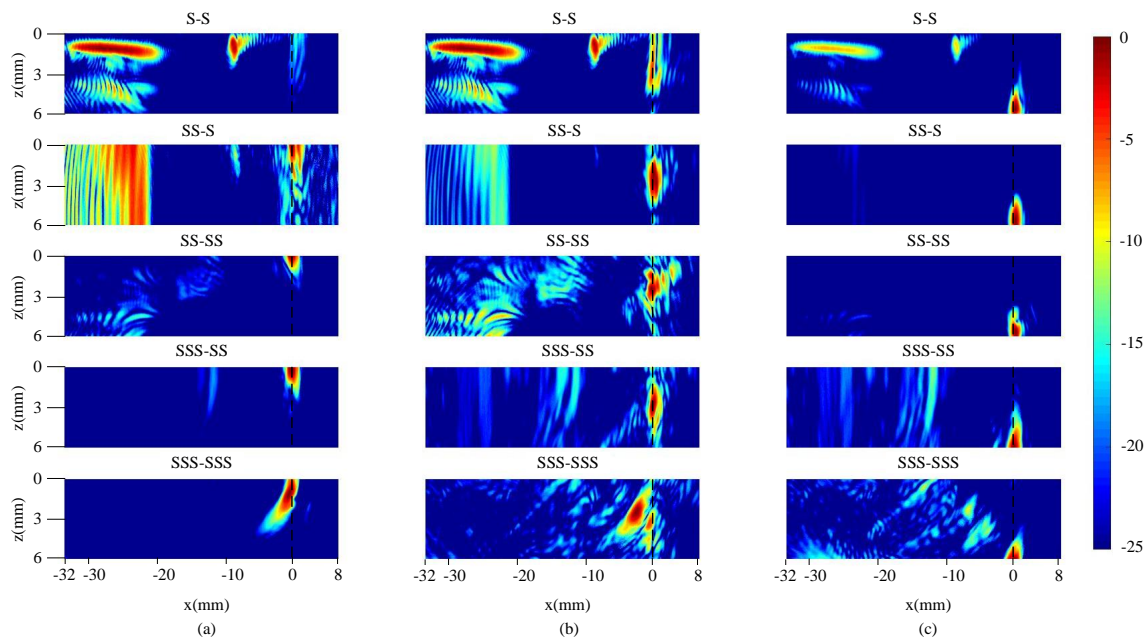**Table 5.** DSNR of circular defects based on the wedge coupling TFM imaging results.

Base Point	S-S	SS-S	SS-SS	SSS-SS	SSS-SSS
(0 mm, 0 mm)	29.93 dB	45.00 dB	53.73 dB	47.24 dB	35.72 dB
(0 mm, 3 mm)	35.31 dB	36.75 dB	47.50 dB	33.17 dB	33.63 dB
(0 mm, 6 mm)	47.64 dB	47.80 dB	51.28 dB	41.96 dB	54.84 dB
Mean	37.63 dB	43.18 dB	50.83 dB	40.79 dB	41.40 dB
Std	9.08 dB	5.75 dB	3.14 dB	7.11 dB	11.69 dB

Figure 10 gives the relations between the maximum SS-SS mode image amplitude of the circular defect and its nominal diameter at different base points. In contrast with direct contact, the amplitude increased significantly at each base point. As a result, the measurement of the circular defect was possible for a diameter greater than 0.8 mm. The amplitude decrement for a diameter smaller than 0.8 mm near the upper surface ($z = 0$ mm) was expected as the gap between the defect and surface was close to the shear wavelength (0.616 mm). The additional diffraction signal obtained by SS-SS mode will finally enhance the maximum amplitude.
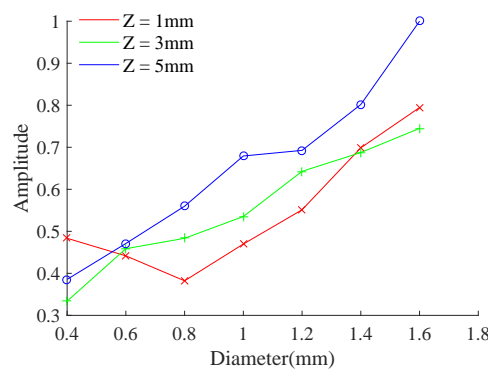
Figure 10. Plot of the maximum defect image value using the SS-SS mode image.

Figure 11 gives the TFM results of rectangular defects at different base points, whose sizes were all 1.0 mm × 0.3 mm. Unlike all the statistical results of DSNR given above, a mode having both the maximum mean value and the minimum standard deviation of DSNR does not exist, as shown in Table 6. Therefore, the imaging performance of the defect was determined by its location: for a defect extended from the upper surface (a), the highest DSNR 55.08 dB occurred in SSS-SS mode; for defect extended from the lower surface (c), the highest DSNR 62.48 dB occurred in SS-S mode; for a defect located in the center (b), both SS-S and SSS-SS had a high DSNR value. The DSNR difference between them was only about 0.39 dB.

Figure 11. Wedge coupling TFM imaging results of rectangular defects at different base points: (**a**) (0 mm, 0 mm); (**b**) (0 mm, 3 mm); (**c**) (0 mm, 6 mm).

Table 6. DSNR of rectangular defects based on the wedge coupling TFM imaging results.

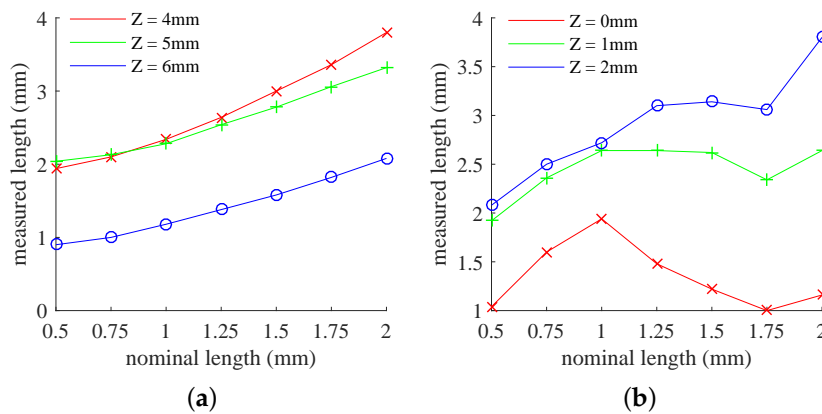| Base Point	S-S	SS-S	SS-SS	SSS-SS	SSS-SSS
(0 mm, 0 mm)	32.20 dB	40.93 dB	53.50 dB	55.08 dB	45.16 dB
(0 mm, 3 mm)	37.51 dB	41.01 dB	37.36 dB	41.40 dB	34.73 dB
(0 mm, 6 mm)	61.95 dB	62.48 dB	58.36 dB	54.49 dB	53.76 dB
Mean	43.89 dB	48.14 dB	49.7 dB	50.32 dB	44.55 dB
Std	15.87 dB	12.41 dB	11.0 dB	7.73 dB	9.53 dB

These observations can be explained according to the geometrical properties of the acoustic ray. When SS-S mode was applied to the upper surface rectangular defect and SSS-SS mode was applied to the lower surface rectangular defect, the angles α and β between reflection acoustic ray and normal vector of coupling interface were too large, as shown in Figure 12. The A-scan signal received by the array transducer in this case will become much smaller according to the relation between the transmission coefficient and the incident angle. As a result, the DSNR of the inappropriate asymmetry mode will become much lower. On the other hand, the SSS-SS mode DSNR of the lower surface defect was greater than the SS-S mode DSNR of the upper surface defect by about 14 dB since β was much smaller than α.

Figure 13a gives the relation between the measured −6-dB drop length of the rectangular defect in the SS-S mode image and its nominal length from $z = 4$ mm to $z = 6$ mm. When the nominal length was not smaller than 1 mm, the significant linearity of each curve allowed us to establish the theoretical sizing equation by linear regression. The input of the sizing equation was the −6-dB

drop length. According to the fitting results listed in Table 7, the slope and intercept of the linear sizing equation were determined by the base point location. For the rectangular defect extended from the lower surface, the sizing equation was approximately equal to the identity function. For a rectangular defect away from the lower surface, the slope decreased rapidly, and the intercept became an unneglectable negative value. Figure 13b gives the relation between the measured −6-dB drop length of the rectangular defect in the SSS-SS mode image and its nominal length in the upper half region. Unfortunately, no significant linearity or monotonicity exists. The measured −6-dB length of the SSS-SS mode TFM image was unable to characterize the upper half region rectangular defect.
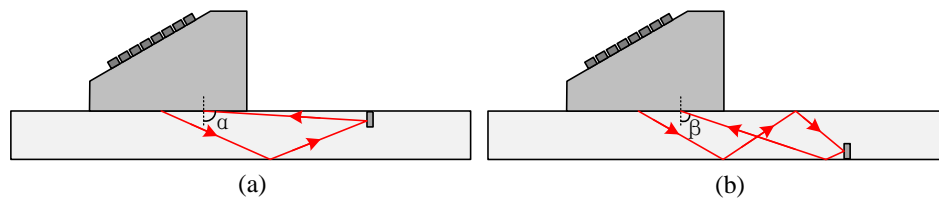
Figure 12. Inappropriate acoustic ray path for rectangular defect inspection: (**a**) SS-S mode for the upper surface; (**b**) SSS-SS mode for the lower surface.

Figure 13. Plot of the measured −6-dB drop length using different mode images: (**a**) SS-S mode; (**b**) SSS-SS mode.

**Table 7.** The −6-dB drop length and fitting result of the sizing equation using SS-S mode.

Base Point	Nominal Length					Fitting Result
	1 mm	1.25 mm	1.5 mm	1.75 mm	2 mm	
(0 mm, 4 mm)	2.34 mm	2.64 mm	3.00 mm	3.36 mm	3.80 mm	$L_{\text{nominal}} \approx 0.6838 L_{-6\text{dB}} - 0.5704$
(0 mm, 5 mm)	2.28 mm	2.54 mm	2.78 mm	3.06 mm	3.32 mm	$L_{\text{nominal}} \approx 0.9611 L_{-6\text{dB}} - 1.1872$
(0 mm, 6 mm)	1.18 mm	1.38 mm	1.58 mm	1.82 mm	2.08 mm	$L_{\text{nominal}} \approx 1.1118 L_{-6\text{dB}} - 0.2878$

The above analyses show that the defect imaging performances and sizing abilities of wedge coupling methods were better than direct contact methods when applied to the thin-walled structure. The geometrical type of defect can be distinguished by comparing both the symmetry and asymmetry mode imaging results. For the circular defect, the best imaging mode was SS-SS; the maximum image amplitude of the circular defect can be used to measure its diameter. For the rectangular defect, the combination of the SS-S and SSS-SS mode image can give the imaging result with the highest DSNR value at an arbitrary depth. In the lower half region, the nominal length of the rectangular defect greater than 1 mm can be measured based on the linear sizing equation and the −6-dB drop length of the SS-S mode image.

4. Experimental Analysis

4.1. Experimental Setup

A real-time experimental system for linear ultrasonic array inspecting was built as shown in Figure 14a. The array controller OEMPA128-128 was provided by Advanced OEM Solutions Company (West Chester, OH, USA). The array transducer and coupling wedge used here had the same parameters as the simulation in Section 3.1. Four aluminum plates (referred to as Plate#1, #2, #3, and #4) with thicknesses of 6 mm were manufactured. For each sample, the section at $x = 0$ was jointed by friction stir welding, where several $\Phi 0.7$ mm SDH and 0.5 mm $\times$ 0.3 mm EDM notches were embedded, as shown in Figure 14b–e. In the following analyses, TFM images are all restricted in the region [−10 mm, 10 mm] $\times$ [0 mm, 6 mm]. To analyze the performance, the artificial defects of SDH and EDM notches were regarded as the circular and rectangular defects introduced in Section 3, respectively. The box region for average DSNR calculation became much smaller since multiple-defects existed in Plate#1–Plate#3. Anisotropy was not considered in this paper since the main topic of this paper was thin-walled structure inspection using the ultrasonic array. It is just a coincidence that our available thin-walled samples with different types of defects were manufactured by stir friction. However, the group velocity variation due to anisotropy may increase the image amplitude of the background, thus decreasing the DSNR value in the experimental result.
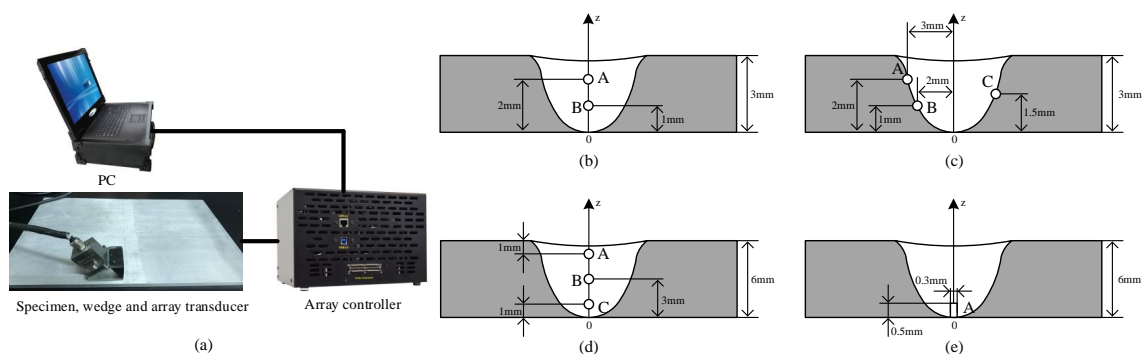

Figure 14. Experimental configuration and testing pieces: (**a**) array system; (**b**) Plate#1; (**c**) Plate#2; (**d**) Plate#3; (**e**) Plate#4.

4.2. Analysis of the Direct Contact Result

Figure 15 gives the direct contact TFM results of Plate#1–Plate#4 using longitudinal modes L-L, LL-L, LL-LL, LLL-LL, and LLL-LLL. The DSNR value of each defect is listed in Table 8.

Unlike the theoretical analysis, the DSNR values of some modes were undefined since defects were not found in their corresponding imaging results. For Plate#1, the two SDHs embedded along section $x = 0$ could both be found at the center of the LLL-LLL mode image with unneglectable background noise. The DSNR of Defects A and B were 3.18 dB and 4.20 dB, which were too low to be used for interpretation. For Plate#2, the image of Defect B was not found among all modes. The highest DSNR of Defects A and C both occurred in LL-LL mode. The LLL-LLL mode image, with three significant spots, gave a completely wrong inspection result since the spot locations did not agree with the SDHs. For Plate#3, only Defect C could be found in the LL-LL and LLL-LL mode images. In the LL-L and LLL-LLL mode images, the amplitudes of the three SDHs along section $x = 0$ mm were mutually overlapped. For Plate#4, the highest DSNR occurred in mode LLL-LL. Due to the complex self-reflections among the multiple defects in Plate#1–Plate#3, only Plate#4 had a reliable testing result. The above analyses validate the conclusion about the best imaging mode in Section 3.2. Furthermore, the poor DSNR and high miss rate of Plate#1–Plate#3 imaging results also showed that direct contact ultrasonic array methods are not recommended for thin-walled structure inspection.
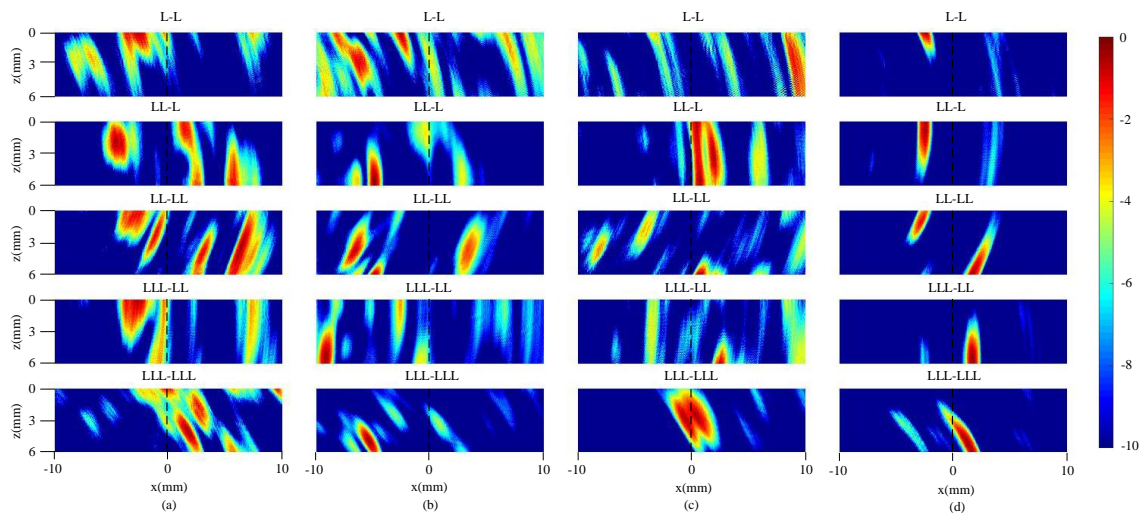
Figure 15. Experimental TFM imaging results of direct contact: (**a**) Plate#1; (**b**) Plate#2; (**c**) Plate#3; (**d**) Plate#4.

Table 8. DSNR of direct contact TFM imaging results.

Base Point	L-L	LL-L	LL-LL	LLL-LL	LLL-LLL
Plate#1 Defect A	undefined	undefined	undefined	undefined	3.18 dB
Plate#1 Defect B	undefined	undefined	undefined	undefined	4.20 dB
Plate#2 Defect A	4.31 dB	undefined	11.20 dB	undefined	undefined
Plate#2 Defect B	undefined	undefined	undefined	undefined	undefined
Plate#2 Defect C	undefined	undefined	8.75 dB	undefined	undefined
Plate#3 Defect A	undefined	undefined	undefined	undefined	undefined
Plate#3 Defect B	undefined	undefined	undefined	undefined	undefined
Plate#3 Defect C	undefined	undefined	6.83 dB	6.14 dB	undefined
Plate#4 Defect A	undefined	undefined	10.76 dB	12.69 dB	8.88 dB

4.3. Analysis of the Wedge Coupling Result

Figure 16 gives the wedge coupling TFM results of Plate#1–Plate#4 using shear modes S-S, SS-S, SS-SS, SSS-SS, and SSS-SSS. The DSNR value of each defect is listed in Table 9. The anisotropy of friction stir welding zone increased the image amplitude of the background by more than 10 dB with respect to the simulation results in Section 3.3. Therefore, the amplitude range for imaging was reduced from $[-25 \text{ dB}, 0 \text{ dB}]$ to $[-15 \text{ dB}, 0 \text{ dB}]$.

Unlike direct contact modes, the best imaging performance of each plate can be obtained. For Plate#1–Plate#2, the highest DSNR values both occurred in SS-SS mode. When SDHs were adjacent, asymmetric mode results had the tendency to regard multiple circular defects incorrectly as a single rectangular defect. For Plate#3, Defect B was not found in all asymmetry mode results. The DSNR differences among S-S, SS-SS, and SSS-SSS were much smaller than the other samples because of the complex self-reflections among multiple defects. It is highly recommended to use multiple symmetry mode results to evaluate the real defect distribution in this case. For Plate#4, although the highest DSNR occurred in symmetry mode SSS-SSS, the asymmetry mode SS-S was preferable due to the distortion and artifact around $x = 5$ mm. The much higher DSNR in the SSS-SSS mode result was caused by the strong root reflection introduced in Section 3.2. The above analyses validate the conclusion about the best imaging mode in Section 3.3. Furthermore, thin-walled structure inspection using SS-SS, SS-S, and SSS-SS mode TFM images simultaneously is not the sufficient condition to discover all existing defects correctly. For samples with multiple defects, additional imaging modes and defect sizing approaches may be needed to improve the detection accuracy.
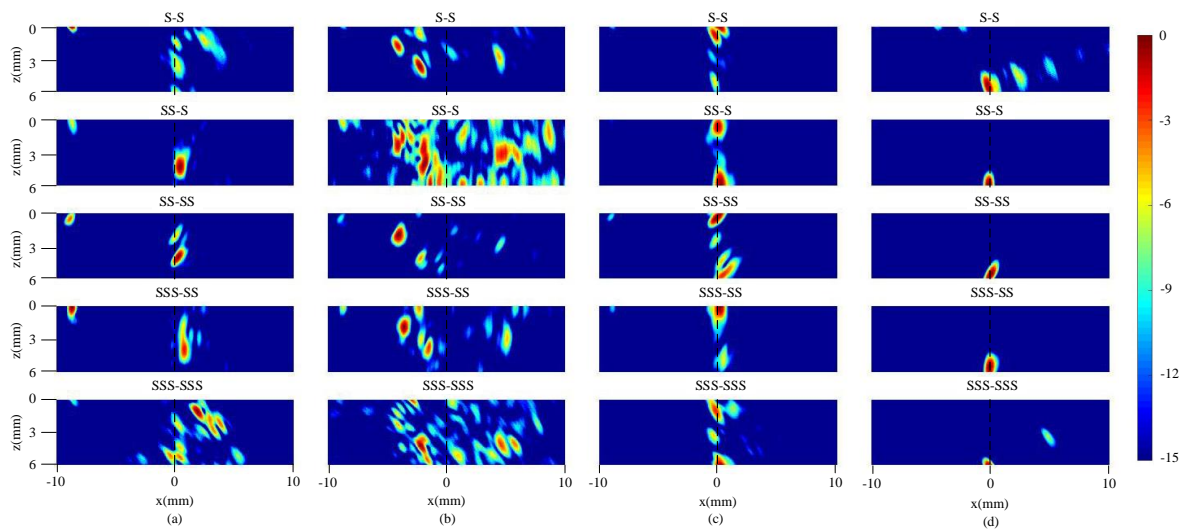
Figure 16. Experimental TFM imaging results of wedge coupling: (**a**) Plate#1; (**b**) Plate#2; (**c**) Plate#3; (**d**) Plate#4.

Table 9. DSNR of wedge coupling TFM imaging results.

Base Point	S-S	SS-S	SS-SS	SSS-SS	SSS-SSS
Plate#1 Defect A	15.67 dB	undefined	35.64 dB	undefined	8.35 dB
Plate#1 Defect B	13.96 dB	27.44 dB	40.45 dB	10.02 dB	5.54 dB
Plate#2 Defect A	25.50 dB	undefined	29.76 dB	23.33 dB	undefined
Plate#2 Defect B	22.79 dB	undefined	25.37 dB	16.29 dB	undefined
Plate#2 Defect C	16.23 dB	undefined	20.38 dB	11.13 dB	undefined
Plate#3 Defect A	20.55 dB	24.56 dB	26.61 dB	21.53 dB	18.43 dB
Plate#3 Defect B	6.53 dB	undefined	13.52 dB	undefined	14.52 dB
Plate#3 Defect C	16.44 dB	22.98 dB	15.69 dB	11.56 dB	17.82 dB
Plate#4 Defect A	24.51 dB	39.96 dB	30.59 dB	32.10 dB	45.08 dB

5. Conclusions

This paper investigated thin-walled structure inspection using different linear ultrasonic array methods. The thickness of the thin-walled structure was smaller than five-times the longitudinal wavelength. Each ultrasonic array method corresponded to a specific TFM imaging mode. The defect imaging performances and sizing abilities of wedge coupling methods were better than those of the direct contact methods. The indicator DSNR was a useful tool to evaluate the imaging performances of different modes.

To inspect an unknown defect, the first step was calculating the DSNR of each imaging mode. If the symmetry mode had the highest DSNR value, the geometrical type of defect would be similar to a circle. On the other hand, if the asymmetry mode had the highest DSNR, the geometrical type of defect would be similar to a rectangle. In the case of a near-circular defect, a diameter larger than 1 mm could be measured according to the maximum image amplitude of the defect. In the case of a near-rectangular defect, if the defect position was close to the lower surface, a nominal length greater than 1 mm could be measured according to the linear sizing equation and the -6-dB drop length of the SS-S mode defect image. The slope and intercept of the linear sizing equation were determined by base point location.

Material anisotropy and complicated self-reflections would increase the image amplitude of the background by about 10 dB. Additional group velocity correction will be considered in the future to eliminate the anisotropic influence. Imaging results of more modes like SSSS-SSS and SSSS-SSSS may also be combined to improve the inspection performance of a sample with a more complicated defect distribution.

References

1. Mignogna, R.; Green, R.E.; Duke, J.C.; Henneke, E.G., II; Reifsnider, K.L. Thermographic investigation of high-power ultrasonic heating in materials. *Ultrasonics* **1981**, *19*, 159–163. [CrossRef]
2. Usamentiaga, R.; Venegas, P.; Guerediaga, J.; Vega, L.; Molleda, J.; Bulnes, F.G. Infrared thermography for temperature measurement and non-destructive testing. *Sensors* **2014**, *14*, 12305–12348. [CrossRef] [PubMed]
3. Kruth, J.P.; Bartscher, M.; Carmignato, S.; Schmitt, R.; De Chiffre, L.; Weckenmann, A. Computed tomography for dimensional metrology. *CIRP Ann. Manuf. Technol.* **2011**, *60*, 821–842. [CrossRef]
4. Blitz, J.; Simpson, G. *Ultrasonic Methods of Non-Destructive Testing*, 1st ed.; Champman&Hall: London, UK, 1996.
5. Schmerr, L.W., Jr. *Fundamentals of Ultrasonic Nondestructive Evaluation: A Modeling Approach*; Springer: New York, NY, USA, 1998.
6. Doyle, P.A.; Scala, C.M. Crack depth measurement by ultrasonics: A review. *Ultrasonics* **1978**, *16*, 164–170. [CrossRef]
7. Drinkwater, B.; Wilcox, P. Ultrasonic arrays for non-destructive evaluation: A review. *NDT E Int.* **2005**, *38*, 701–711. [CrossRef]
8. Felice, V.; Velichko, A.; Wilcox, D. Accurate depth measurement of small surface breaking cracks using an ultrasonic array post-processing technique. *NDT E Int.* **2014**, *68*, 105–112. [CrossRef]
9. Holmes, C.; Drinkwater, B.W.; Wilcox, P.D. Post-processing of the full matrix of ultrasonic transmit-receive array data for nondestructive evaluation. *NDT E Int.* **2005**, *38*, 701–711. [CrossRef]
10. Weston, M.; Mudge, P.; Davis, C.; Peyton, A. Time efficient auto-focussing algorithms for ultrasonic inspection of dual-layered mMedia using full matrix capture. *NDT E Int.* **2012**, *47*, 43–50. [CrossRef]
11. Zhang, J.; Drinkwater, B.; Wilcox, P. Efficient immersion imaging of components with nonplanar surfaces. *IEEE Trans. Ultrason. Ferroelectr. Freq. Control* **2014**, *61*, 1284–1295. [CrossRef] [PubMed]
12. Zhang, J.; Drinkwater, B.; Wilcox, P. The use of ultrasonic arrays to characterize crack-like defects. *J. Nondestruct. Eval.* **2010**, *29*, 222–232. [CrossRef]
13. Miller, G.F.; Pursey, H. The field and radiation impedance of mechanical radiators on the free surface of a semi-infinite isotropic solid. *Proc. R. Soc. Lond. A* **1954**, *223*, 521–541. [CrossRef]
14. Wooh, S.; Shi, Y. Influence of phased array element size on beam steering behaviour. *Ultrasonics* **1998**, *36*, 737–749. [CrossRef]
15. Lee, J.; Choi, S. A parametric study of ultrasonic beam profiles for a linear phased array transducer. *IEEE Trans. Ultrason. Ferroelectr. Freq. Control* **2000**, *47*, 644–650. [PubMed]
16. Zhang, J.; Drinkwater, B.; Wilcox, P. Defect characterization using an ultrasonic array to measure the scattering coefficient matrix. *IEEE Trans. Ultrason. Ferroelectr. Freq. Control* **2008**, *55*, 2008–2264. [CrossRef] [PubMed]
17. Mahaut, S.; Leymarie, N.; Poidevin, C.; Fouquet, T.; Dupond, O. Study of complex ultrasonic NDT cases using hybrid simulation method and experimental validations. *Insight* **2011**, *53*, 664–667. [CrossRef]
18. *CUDA C Programming Guide*; NVIDIA Corporation: Santa Clara, CA, USA, 2018.
19. Xu, N.; Zhou, Z. Numerical simulation and experiment for inspection of corner-shaped components using ultrasonic phased array. *NDT E Int.* **2014**, *63*, 28–34. [CrossRef]
20. Thomas, J.W. *Numerical Partial Differential Equations: Finite Difference Methods*; Springer: New York, NY, USA, 2013.